This is an Accepted Manuscript of an article published by Taylor & Francis in Heat Transfer Engineering on 19/10/2022, available at https://www.tandfonline.com/doi/10.1080/01457632.2022.2134075

Effect of Thermal Boundary Conditions and Turbulence Treatment on the Simulated Performance of a Ribbed Heat Exchanger

ABSTRACT

Ribbed surfaces are widely employed in heat exchangers to enhance the convective heat transfer and hence the overall thermal efficiency. This study aims to investigate the importance of two important approximations used in computational fluid dynamics simulation, i.e. the thermal boundary conditions and the turbulence modeling, using a popular test case for the heat transfer over a continuous ribbed plate was taken as a reference. Numerical simulations were performed both neglecting and considering the conduction within the solid, to verify the effect of different thermal boundary conditions on the fluid domain, and with several turbulence treatments, ranging from common Reynolds-averaged Navier-Stokes approaches to higher fidelity but more computationally intensive Large Eddy Simulations. The results demonstrate that both aspects are important for an accurate prediction of the thermal performance of ribbed channels.

Introduction

The use of aerodynamic appendices, such as ribs, fins and pins, represents an effective method to increase the performance of heat exchangers and produce a more economical thermal system design. In plate heat exchangers, ribs can be placed on one or two opposite surfaces of the channel in a staggered arrangement, transverse to the main direction of the incoming flow or angled according to a V-shape configuration [1]. Their scope is to increase the turbulence close to the wall and to interrupt the thermal boundary layer, thus enhancing the heat transfer with respect to the flow over a smooth surface. At the same time, the perturbation of the core flow causes an increase

in the pressure drop and, consequently, in the pumping power required Error: Reference source not found.

Over the years, significant efforts have been devoted to the investigation of the optimal configuration of roughened surfaces. Many works have focused on studying the influence of the geometry (in particular rib height *e* and pitch *p*) on the heat transfer coefficient [3][4], also under pulsating flow regimes [5] and in rotating channels [6]. Liu *et al*. [7] studied the use of extended surfaces on the absorber plate of a solar collector, and developed a correlation between the Nusselt number and the increase in pumping factor. Prasad and Saini [8] showed that Nusselt number and friction factor increase with the relative roughness height and decrease for larger relative roughness spacing (p/e), although not in the same proportion. Furthermore, they showed that for a fixed relative roughness height, the average Nusselt number increases with the Reynolds number, while the friction factor approaches a constant value [9].

Webb [10] studied the behavior of the flow over a surface with constantly spaced ribs, and described it as a problem dominated by boundary layer separation and reattachment. The flow separates after each rib and the reattachment occurs only if the relative pitch distance p/e between two successive ribs is larger than about 8. Measurements revealed that the heat transfer coefficient reaches its maximum value close to the reattachment point and, therefore, even a very compact ribs configuration should be avoided in order to maximize the heat transfer rate. On the contrary, for $p/e>10$, a new boundary layer forms before the following rib, thus resulting in a decrease in the average heat transfer rate.

Experimental studies have been performed on different geometrical configurations, also obtained as a combination of different types of ribs and vortex generators. The performance of thermal systems

has been evaluated based on temperature measurements carried out mainly by means of thermocouples [11][12][13][14], thermochromics liquid crystals (TLCs) [15][16][17] [18][19][28] [20] or infrared cameras [21][22]. Among these, Tanda's studies [15] on ribbed channels are of great importance for the scopes of the present work, as they provide relevant experimental data to validate numerical simulations. Tanda used TLCs to obtain detailed maps for the heat transfer coefficient in rectangular channels equipped with transverse continuous, broken ribs and V-shaped broken ribs, at various Reynolds' numbers [15]. The thermal maps revealed a strong dependence of the heat transfer distribution on the ribs' shape and arrangement. The transverse continuous ribs exhibited a periodic Nusselt distribution after the fourth rib, with a maximum at the flow reattachment point after each rib. The transverse broken ribs in a staggered arrangement provided higher Nusselt numbers, with a mean value that increased by reducing p/e. The Nusselt numbers for the V-shaped broken configurations were shown to be locally dependent on the apex angle and on the p/e ratio, but the average performance appeared to be insensitive to the V-ribs apex angle.

Several experimental activities have also been performed in conjunction with numerical simulations, to provide a detailed investigation of the fluid-dynamics phenomena generated by the ribs. Hagari *et al.* [13] studied the heat exchange in a rectangular channel representative of a combustor liner cooling passage equipped with W-shaped miniature ribs located on one side. Similarly, Li *et al.* [14] studied W-shaped miniature ribs together with transverse, angled and V-shaped geometries, concluding that, among them, the W-ribs are the most effective configuration, with a thermal efficiency of about 2.2 in the range Reynolds' numbers studied. Baggetta *et al.* [16] made use of longitudinal ribs in high aspect ratio rectangular channels to enhance the secondary vortex responsible for increased heat transfer. Satta *et al.* [17] studied the effect of the entrance geometry on the performance of ribbed heat exchangers. Liu et al. [18] studied different truncated

ribs configurations, obtained as the fractal evolution of continuous ribbed channels. Rao and Zhang [19] combined V-shaped ribs and dimples to improve the heat transfer in cooling channels representative of the ones used in gas turbine engines. Kaewchoothong *et al.* [20] performed both experimental tests and numerical simulations on a square channel equipped with ribs on two opposite surfaces. The study focused on different arrangements, showing that an inclined setting promotes higher average Nusselt numbers than transverse configurations.

The majority of numerical simulations available in the literature are based on the solution of the Reynolds-Averaged Navier-Stokes (RANS) equations, in combination with different turbulence models. Eiamsa-ard and Changcharoen [23] employed the SST k- ω model to study a channel with different rib geometries, with the aim of reducing the flow separation and extending the reattachment area with respect to the more conventional squared rib configuration. Boulemtafes-Boukadoum *et al.* [24] compared the shear stress transport (SST) k-ω model with three other turbulence models, i.e. standard k-ω, k-ε and k-ε renormalization group (RNG), with the purpose of investigating the convective heat transfer enhancement in a solar air absorber fitted with rectangular ribs. Among all models tested, the SST k-ω model provided predictions of the Stanton number best fitting the experimental data, especially for Reynolds' numbers larger than 5,000. Ma *et al.* [25] investigated the influence of inlet flow temperature and ribs height on the performance of heat exchangers operating at high temperature. Two different turbulence models were tested, the standard k- ε and the Reynolds stress model (RSM). The comparison against experimental data revealed that the RSM model was able to provide more accurate predictions of the flow structures and of the heat transfer rate in the channel. Akcayoglu and Nazli [26] compared different turbulence models in the prediction of the fluid flow in triangular ducts with vortex generators (VG), and used the most appropriate model (k-ε RNG) to compare the thermal performance of

different VG configurations. Ali *et al.* [27] investigated the effect of similar aerodynamic appendices and of their relative position in rectangular channels, at low Reynolds' numbers (below 300). Wang *et al*. [28] studied the aerodynamic and thermal performance of rectangular ribbed channels at relatively large Reynolds' numbers (20,000-45,000), both with experimental and numerical approaches. Azfal *et al*. [29] performed the optimization of a rectangular channel with periodic ribs, combining a Particle Swarm optimizer with a Neural Network response surface constructed using data from CFD evaluations with a SST k-ω turbulence closure. Chokphoemphun *et al.* [30] studied the effect of different rib geometries on the performance of an air heater, using k-ε RNG as the turbulence model.

Recently, Zheng *et al.* [31] [32] exploited Tanda's measurements [15] for the 0.15 rib-to-channel height, transverse continuous ribs configurations, at both *Re* 8,900 and *Re* 28,500, to investigate the accuracy of a 3D RANS-based numerical approach for simulating the heat exchange in ribbed channels. The ribbed plate was modeled as a uniformly heated zero thickness surface (shell plate) exposed to the airflow, hence neglecting the heat transfer within the plate itself. The Nusselt number distributions predicted using different turbulent models were compared with the experimental data along the plate centerline, finding that numerical curves estimated with the SST Gamma-ReTheta and the SST k-ω models presented maximum values in good agreement with the measured data in the inter-ribs central zone. However, every turbulence model presented a significant underestimation of the heat transfer in the vicinity of the ribs, which was not observed in the experiments. Similar results may be found in the work published by Eiamsa-ard *et al*. [23] on 2D numerical domains.

The discussion on the most appropriate turbulence model for such complex fluid dynamic problems is still open. At the same time, the limits of the RANS approach in providing an accurate evaluation

for a flow with large separations and reattachments become more evident. In fact, the effectiveness of a turbulence model is highly dependent on its capability in approximating the energy transfer in complex flows. Large Eddy Simulations (LES), on the contrary, solve the larger vortex scales explicitly, while only modeling the smaller scales, which are less dependent on the global flow phenomena and therefore easier to approximate. Despite a significantly larger computational cost, their use can provide valuable insights for understanding the complex phenomena involved.

Nowadays, the ever increasing availability of computational power is sustaining the use of LES simulations in the study of a wider range of heat transfer enhancement methodologies, including ribbed channels for cooling electronic boards (Liu *et al*. [33]), winglet pair vortex generators (Bjerg *et al.* [34]), combination of delta-winglet vortex generators and longitudinal riblets for improving the performance of plate solar receivers (Colleoni *et al.* [35]). Recently, Toubiana *et al.* [36] made use of LES to produce a detailed description of the complex flow structures resulting from the laminar to turbulent flow transition in an elliptical finned-tube heat exchanger. Peltonen *et al.* [37] combined LES and experimental measurements to investigate the effect of both plate and pin fin heat exchangers on the internal flow in a pipe, and the consequent effect on the heat transfer rate. While a good agreement was found between the numerical and the experimental flow fields, the prediction of the overall performance was shown to be sensitive to the thermal boundary condition applied on the surfaces of the heat exchangers. The authors concluded that a realistic temperature distribution is of primary importance to model the heat transfer rate accurately and suggested that conjugate heat transfer simulations could represent a more effective approach for the evaluation of the thermal performance of heat exchangers.

This paper investigates the capability of different computational fluid dynamics (CFD) approaches in the simulation of the heat exchange inside a rib-roughened channel. An experimental test

performed by Tanda [15] on a continuous transverse ribbed plate at a Reynolds' number of 8,900 is taken as a reference. The study focuses on two aspects:

a) the influence of the heat exchange within the solid plate on the evaluation of the thermal performance of the ribbed channel. The presence of the heated plate is simulated using both a shell representation, with the effect that the heat flux boundary condition is applied directly to the fluid, and considering its actual thickness, hence allowing the heat flux to redistribute inside the plate as calculated by a conjugate heat transfer approach. Initially, 2D steady RANS simulations, with different turbulence models from the k-ε and k-ω groups, are analyzed, with particular attention to the effect of the thermal boundary conditions. Simulation results are then compared with experimental data in terms of Nusselt number on the plate surface, highlighting the impact of different turbulence models and simulation assumptions.

b) In order to evaluate the inaccuracies introduced by turbulence modeling in the prediction of the complex flow in a ribbed channel, 3D LES simulations for the same thick plate configuration are compared with RANS results. Since the heat exchanges within solid and fluid domain are characterized by very different times scales, a multi-step decoupled procedure is employed for the conjugate heat transfer. A detailed description of the procedure is reported, together with a comparison of the fluid and thermal fields predicted by LES and RANS approaches, highlighting the differences and limitations of common turbulence models.

The rest of the paper is organized as follows. First, the numerical setup used in RANS simulations is presented, together with the results and a comparison with experimental data. Then, the approach

used in LES simulations is introduced, together with an analysis of the results. Finally, the main conclusions of this work are summarized.

RANS simulations

The RANS simulations aim to reproduce the experimental measurements performed by Tanda [15] on a rectangular channel equipped with plexiglas ribs on the lower surface. Among the different tests reported in [15], the one characterized by continuous transverse rectangular ribs with rib to channel height ratio of 0.25, pitch length to rib height $p/e=8$ and an air flow at $Re_{D_h}=8{,}900$ was selected as test case for validation of different turbulence models. All CFD simulations were carried out by means of the finite-volume commercial code Ansys Fluent 17, while the meshing tool Ansys Icem CFD was used to generate the geometrical domain and its spatial discretization.

Numerical model

Given that three-dimensional features are not expected in the mean flow [31], RANS simulations were performed on a 2D computational domain corresponding to the mid longitudinal plane of the test section (Figure 1). Two additional straight channels with length of approximately $6H$ were added to the opposite ends to limit the influence of the boundary conditions on the internal flow field. A pressure inlet boundary condition (total pressure and temperature specified) was applied to the inlet section, with a fully developed total pressure profile (Figure 1) set to generate an air flow at $Re_{D_h}=8{,}900$, a total temperature equal to 293.15 K, a turbulence intensity of 10% with a correlation length of 1.74 mm. A reference value of $1.013 \cdot 10^5$ Pa was fixed as pressure outlet condition on the opposite end of the domain (fixed static pressure). The air was modeled as an ideal gas with thermodynamic properties (specific heat, viscosity and thermal conductivity) that varied with temperature by means of properly implemented laws.

Two different approaches were used to investigate the effect of the thermal distribution through the plate thickness (Figure 2): the first one modeled the plate as a shell plate with zero thickness,with the effect that the specified constant heat transfer rate (500 W/m^2) was directly applied to the surface exposed to the air-flow (as in other works such as [23], [25] and [32]); the second approach simulated a fixed thickness plate with the same constant heat transfer rate imposed at its bottom surface. The last approach is more representative of the actual experiment [15]: the heated steel plate was modeled as a 0.5 mm thick solid region (density $\rho = 8030\, kg/m^3$, specific heat $c_p = 502.5\, J/kg\,K$, thermal conductivity $\lambda = 16.3\, W/m\,K$), as reported in [15]. The heat exchange through the upper ribbed surface, in contact with the flow,resulted from the evaluation of both the fluid and solid thermal fields, i.e. from a conjugate heat transfer analysis. In both approaches, the ribs were considered as made of insulating material (adiabatic wall), as schematically shown in Figure 2. All remaining walls were also treated as adiabatic.

RANS simulations were performed by means of a steady approach, using second order centered schemes for diffusive fluxes and a QUICK scheme for convective fluxes. The SIMPLEC algorithm was employed for pressure correction. Five turbulence models were considered to close the system of equations, belonging to the *k*-ε and *k*-ω models groups: *k*-ε, RNG *k*-ε, Realizable *k*-ε, *k*-ω and SST *k*-ω.

Computational grid

The domain was discretized by means of a structured grid, refined in the vicinity of the lower and upper surfaces and around the ribs to properly solve for the wall boundary layer. The latter requires a non-dimensional wall distance ($y^+ = \frac{y\sqrt{\rho \tau_w}}{\mu} y^+$) lower than unity, as verified in, Figure 3a. The cell size increases away from the wall with a maximum growth rate of 1.1. The optimal mesh resolution

was selected by means of a grid convergence analysis on 2D RANS simulations. Results for the SST k-ω turbulence model are reported in Figure 3, but similar results were obtained with other turbulence models. The plot in Figure 3b presents the convergence of the average Nusselt number (non-dimensionalized with the corresponding asymptotic convergence value), obtained with 9 different grids resulting from a uniform refinement, starting from a datum mesh. Every successive mesh was obtained multiplying the number of edges by a factor of 1.5 in every direction, thus obtaining discretized domains ranging from about 1,000 to 855,000 cells. Figure 3c presents the relative error as a function of the average linear mesh size, in logarithmic scale, so that the slope of the curve is representative of the approximate convergence order. Order of convergence and grid convergence index (GCI) have been calculated following the procedure reported in [38] and summarized in [39], using 4 different mesh triplets (Table 1). The mesh composed of 33,508, with a GCI of 1.1%, has been considered sufficient for the purposes of this work, and was therefore adopted for the following RANS simulations.

RANS results

The temperature distributions predicted by the RANS simulations with different turbulence models, both including and neglecting the heat transfer within the solid, were processed to obtain the Nusselt number variations on the plate according to the following equations:

$$h = \frac{\dot{q}_w}{T_w - T_{air,x}} \qquad (1)$$

$$Nu = \frac{h D_h}{\kappa} \qquad (2)$$

where $\dot{q}_w$ is the wall heat flux, assumed as uniformly distributed over the plate, as in the reference experiment [15], T_w the local temperature on the plate, $T_{air,x}$ the air temperature in the flow core at

distance x from the inlet section, and D_h is the hydraulic diameter of the channel. Finally, κ is the thermal conductivity of air. RANS results were compared against Tanda's experimental data [15], as shown in Figures 4a and 4b for the shell plate and the thick plate approaches, respectively. Experimental uncertainties (estimated as 5.6% of the reported Nusselt value [15]) are superimposed to the experimental values in Figure 4. The Nusselt number distribution predicted with the shell plate model closely resembles the results reported in the scientific literature for a similar numerical approach ([23], [25] and [32]): a concave curve in the inter-ribs space, delimited by sharp variations near the ribs. All the turbulence models tested predicted average Nusselt numbers lower than the ones given by measurements, but with ranges of variation (from about 10 up to 90) significantly larger than in the experimental distribution (where it ranged from about 55 to 75). All numerical curves, with the exception of the SST k-ω curve, present pronounced peaks in Nusselt numbers just upstream of the leeward face of each rib, while a unique, and less evident, peak exists in the experimental curve at $x/D_h = 4$. Among the different turbulence models considered, the ones from the k-ε groupprovide a better estimate both for the average Nusselt number and for the range of variability, i.e. the ratio of maximum to minimum Nusselt number. In particular, the RNG k-ε presents the lowest relative error for the average Nusselt number (24%).

Conversely, the numerical curves obtained with the thick plate approach show a general trend that is remarkably similar to the experiments: a maximum value in Nusselt number is observed in the region between two successive ribs, where the flow reattachment is expected. Then, its value decreases near each rib, but not as sharply as with the previous model: the ratio of maximum to minimum Nusselt number is in good agreement with the measured data (within 1.33-1.44). However, all the predicted average Nusselt numbers are significantly lower than the measured values (ranging from 38.7 up to 46.6); k-ε based models provided Nusselt values higher than k-ω

models along the entire plate centerline, although significantly lower than the experimental values. An investigation on the reasons for the differences between the predictions of turbulence models tested will be presented in the Section “LES results and discussion”.

Both approaches (shell and thick plate), with all turbulence models, predicted Nusselt number distributions well outside of the experimental uncertainty band (see Figure 4). Nevertheless, the shell plate approach proved to be more accurate in predicting the average Nusselt value, while the thick plate modeling better approximates the general trend of the experimental curve, in particular where the flow approaches the ribs. This fact is further confirmed by the analysis of the maximum to minimum Nusselt ratio: as shown in Table 2, values of this parameter in good agreement with experimental data have been provided with all the turbulence models for the thick plate simulations. On the other side, the thermal distributions for the shell plate model cause large variations in Nusselt number across the ribs, which is reflected in an increase of the Nusselt ratios up to a value of 5.60 and with a relative difference with respect to experimental data larger than 130%.

The different response of the two modeling approaches can be explained by observing the distribution of the main thermal parameters on the plate. A comparison in terms of local heat flux and temperature is proposed in Figure 5a and 5b, respectively, for the k-ε turbulence model. As already illustrated, the convective heat exchange is governed by the fluid dynamic behavior of the main flow in the test channel. Imposing a fixed heat transfer rate on the plate surface exposed to the flow, as in the shell plate approach, forces the local temperature to rise in the regions of less effective thermal exchange (i.e. near the ribs), and is the cause of the large variations in surface temperature reported in Figure 5b and consequently in Nusselt number (as already shown in Figure 4), as the Nusselt number in [15] was calculated assuming a constant heat flux on the surface (see

Eqs. (1) and)2)). On the contrary, in the thick plate model, the heat transfer rate is imposed on the bottom surface of the plate, in a manner that is more representative of the actual experimental setup. This has the effect of causing a redistribution of the heat transfer rate, by means of the thermal diffusion within the plate, producing a more even temperature distribution on the upper plate surface (Figure 5b), which leads to the lower variability in Nusselt number shown in Figure 4. It is important to note the difference between the actual local Nusselt number and the Nusselt number evaluated by Tanda [15] with Eqs.(1) and (2): the actual Nusselt number is representative of the plate's local heat exchange and it should not depend in a first approximation on the particular model (shell plate/thick plate) adopted; the Nusselt number evaluated using Eqs. (1) and (2) assumes a constant value for the heat flux, thus depending only on the temperature field, regardless of the real heat transfer rate through the upper surface of the plate. This result is in agreement with the findings of Peltonen *et al*. [37], who studied the effect of thermal boundary conditions on the simulated performance of heat exchangers, suggesting the use of a combined fluid/solid (i.e. conjugate heat transfer) simulation, to avoid the use of an inaccurate temperature or heat flux boundary condition on the fluid domain, which could have a large effect on the results.

The RANS results suggest that the thick plate approach is a closer representation of the experimental setup, while the differences found in the estimation of the average Nusselt number with respect to the measured data could be ascribed to deficiencies of the turbulence modeling in representing the complex mixing in a largely separated flow. Indeed, the convective heat exchange is highly dependent on the complex 3D vortical structures generated by the flow interaction with the ribs, characterized by a series of separation and reattachment phases. In this scenario, the eddies are the main responsible for the mass, momentum and energy transport through the flow field and it is possible that RANS approaches, having been developed for the simulation of attached boundary

layers with limited separation [40], could well be unsuitable for the estimation of the heat transfer in such a complex environment.

The difference between the experimental Nusselt number and the RANS predictions may depend on an inaccurate approximation of the turbulent phenomena, and a Large Eddy Simulation (LES) approach may provide an improved estimation. The LES technique allows to directly solve for the large scale turbulence, limiting the use of modeling to the approximation of the small eddies, which are more isotropic and hence easier to model. In order to test this hypothesis, the same experimental setup was simulated numerically through a thick plate LES approach.

LES

Numerical model

LES simulations were performed on a 3D computational domain representative of a mid longitudinal section of the test channel (Figure 6), created as an extrusion of the 2D domain adopted in the previous thick plate RANS simulations. Given the inherent three-dimensional nature of turbulence and the fact that LES aims to solve the majority of the turbulent scales (only the smallest ones are modeled), a 3D time-dependent approach is required, which causes a significant increase in computational time with respect to RANS simulations. The same boundary conditions scheme used for 2D RANS simulations (Figure 1) was applied to the boundaries of the 3D domain, with the addition of a periodic boundary condition on the lateral surfaces. Moreover, inlet turbulence was injected by means of the vortex method, with a number of vortices equal to 190, an intensity of 10% and a subgrid kinetic energy of 1 m^2/s^2, following the guidelines in [41]. The Kinetic-Energy Transport subgrid-scale model was adopted for modeling the subgrid-scale stresses resulting from the LES filtering operation. The choice was guided by its capability to provide a

more accurate turbulence prediction with respect to the alternative approaches, deriving from a direct modeling of the subgrid-scale turbulence kinetic energy (k_{SGS}) transport [41].

A SIMPLEC scheme was used as the pressure correction scheme, a least squares cell-based evaluation for the gradients. The bounded central differencing was used as the spatial discretization method for the convective terms in the momentum equation, while the QUICK scheme was selected for the subgrid kinetic energy. A 2nd order upwind interpolation was employed for all other equations, while a second order centered scheme was used for all diffusive fluxes.

A transient pressure-based approach with a second order bounded scheme was used for temporal discretization, with a constant time step of $4.8 \cdot 10^{-5}$ s and 20 sub-iterations, in order to ensure a Courant number lower than unity everywhere in the domain. A drop of the residuals of at least 3 orders of magnitude was achieved at every time step. These settings required about 2,500 time increments for completing a fluid passage through the entire domain, corresponding to a physical time of 0.12 s. Simulation were run on a 6 node dual E5-2667 v2 Xeon cluster, and required approximately 40 s per time step for the larger mesh tested.

Since the heat exchange inside the plate occurs with a characteristics time scale significantly larger than convective phenomena in the flow, a very large number of flow passages would be needed in order to achieve a fully developed thermal distribution in the plate. In fact, while the heat transfer in the channel is mostly guided by the velocity v of the main flow, the conductive heat transfer rate inside the plate strictly depends on the thermal diffusivity α of the plate material:

$$\alpha = \frac{\lambda}{\rho c_p} \qquad (3)$$

Therefore, the time scale ratio tr between the convection and the conduction for the specific

scenario was conservatively evaluated with reference to the ribs pitch ($p = 40\,mm$), by means of the following formulation:

$$tr = \frac{p \cdot v}{\alpha} \qquad (4)$$

Based on the aforementioned considerations, a value of tr equal to about 48,500 was obtained, thus indicating that a fully-developed solution for both thermal and fluid dynamics would require about $20 \cdot 10^6$ time increments to be completed in a single coupled solid-fluid simulation, and a computational time not feasible with the existing computing resources. Therefore, the problem has been decoupled by means of an ad-hoc multi-step procedure (similar to the approach proposed in [43]) whose details will be explained in a dedicated section, consisting in alternating the solution of the fluid dynamic field in the channel (with a LES simulation) and of the heat exchange inside the plate (with a dedicated steady thermal solid simulation).

Grid construction

The LES computational grid was defined according to the turbulence integral length scale criterion: LES simulations require larger turbulent eddies to be resolved by the computational grid, while the ones smaller than the grid cells are filtered. The grid cell size should therefore be set to solve a good fraction of the turbulent kinetic energy *k*, while the remainder is modeled. Tyacke and Tucker [40] suggest that about 80% of *k* needs to be solved by the LES approach for the results to be reliable. This requirement was ensured by performing a preliminary 3D steady RANS simulation and evaluating the minimum value of the integral length scale l_0, defined as:

$$l_0 = \frac{k^{1.5}}{\varepsilon} \qquad (5)$$

where ε represents the turbulent kinetic energy dissipation rate. Then, $l_0/5$ was imposed as the

limiting value for the maximum cell size, as suggested in [41] and [42]. The grid was refined in the vicinity of the solid surfaces in order to ensure $y^{+} < 1$. Cells in the vicinity of the walls have an aspect ratio of 1.1 and thus non-dimensional distances in the other directions are of the same order of magnitude.

The domain width W was determined by means of a sensitivity analysis based on three different extrusion lengths: 1, 2 and 4 channel heights (mesh sizes ranging from 3.2 to 12.8 million cells). A constant wall temperature of 300 K was imposed at the lower wall, while the inlet flow total temperature was fixed to 293.15 K. All other walls were treated as adiabatic. For each domain, the instantaneous average heat flux from the channel's lower wall is reported in Figure 7a: the flow stabilizes after about 1 characteristic time, and a width of twice the channel height is sufficient for the turbulent structures' development not to be affected by the periodic boundary conditions. To further support this conclusion, following the approach in [44], the correlation coefficient C for the velocity magnitude was calculated along the transverse direction $\vec{w}$, on a line placed mid-way between the third and fourth rib, at the same height of the rib upper edge.

$$C(\vec{x}, s) = \frac{R(\vec{x}, \vec{x} + s\vec{w})}{R(\vec{x}, \vec{x})} \qquad (6)$$

where $\vec{x}$ is a generic point and $\vec{w}$ a unit vector in the transverse direction. R is calculated as follows for the velocity magnitude v:

$$R(\vec{x}, \vec{x} + s\vec{w}) = \frac{1}{\tau} \int_{t}^{t+\tau} \overline{v(\vec{x})\, v(\vec{x} + s\vec{w})}\, dt \qquad (7)$$

The correlation length can then be estimated using:

$$L = \int_0^W R(\vec{x}, \vec{x} + s\,\vec{w})\,ds \qquad (8)$$

Average heat flux and correlation length in the transverse direction estimated with the 3 domains with increasing width on height ratios are reported in Table 3. Both average heat transfer and correlation length appear to become insensitive to the width of the domain after $W/H = 2$. The correlation length is also significantly smaller than the domain width (Figure 7b), and hence the domain width $W/H = 2$ has been selected for the following simulations.

Multi-step decoupled procedure

In the experiments of Tanda [15], taken as a reference for this work, the heat is supplied by a plane heater flushed to the bottom surface of a stainless steel plate. The heat flux and temperature distribution on the upper surface of the steel plate (which is in contact with the flow) is a result of the combined effect of the thermal exchange within the solid, and of the heat extracted by the flow. As mentioned in Section "Numerical Model", the time scales of the thermal exchanges within solid and fluid domains are orders of magnitude apart, thus requiring an extremely large computational time to reach a fully developed state in a coupled conjugate heat transfer simulation. The alternative approach used was to perform the simulations of the two domains separately, and ensure coupling at the interface, through an iterative procedure. The latter was subdivided in a preliminary initialization step and in a subsequent decoupled cycle (Figure 8): during the preliminary step, a RANS simulation was performed to provide an approximation of the fluid dynamics field for the first LES initialization. The subsequent decoupled cycle involved the alternate execution of LES for the fluid and steady thermal solid simulations. The LES allowed the evaluation of the convective heat exchange for a given thermal distribution inside the steel plate. Each LES was performed until the completion of four flow passages through the entire domain (a total of 10,000 time steps): the first one to obtain a fully developed flow field and the other three for averaging the main flow parameters over time. Each LES simulation required approximately 60 hours on a 6 node dual E5-2667 v2 Xeon cluster.

The solid simulations allow updating the thermal profile inside the plate on the basis of the convective heat exchange with the airflow. At the scope, an additional model was built to solve the heat exchange in the ribbed steel plate. The solid geometry consisted in a longitudinal section of the steel ribbed plate as wide as the LES domain (W), discretized by means of a structured mesh of

about 164,000 hexahedra (Figure 9). The time-averaged *h* profile predicted by the previous LES, together with the fluid temperature, was adopted as thermal condition on the plate ribbed surface, while a uniform heat flux of 500 W/m^2 was imposed at the bottom for simulating the heater effect. Then, the thermal distribution derived from the solid simulation was imposed back to the LES simulation, and the procedure was continued until convergence.

Convergence was considered to be achieved once the difference between the difference between the heat through the upper surface of the plate (in contact with the fluid) and the one set at its bottom surface (as a boundary condition) was below a predefined threshold of 3% (see Figure 8).

LES results and discussion

The decoupled procedure converged after four loops, when the last LES simulation reached the physical time of 1.92 s. A total of 16 passages of the airflow through the numerical domain were simulated, obtaining an average convective heat flux on the upper plate surface equal to 484.9W/m^2 (Figure 10). This value represents the difference between the heat flux imposed on the solid bottom surface (500 W/m^2), where the heater was placed, and the heat dissipated through the ribs. The ribs were modeled both as a low conductivity material (Plexiglass has a thermal conductivity of about 0.18 W/mK, 90 times smaller that the one of the steel plate) and as adiabatic (as assumed in the experiment [15]). No appreciable different were found, as reported in Figure 13.

Upon completion of the last loop, a further mesh quality verification was performed based on the analysis of the solved turbulent kinetic energy fractionk_l, as suggested in [40]. This parameter is defined as the ratio between the average turbulent kinetic energy directly solved by the LES ($\overline{k_{RES}}$) and the average total turbulent kinetic energy:

$$\overline{k_l} = \frac{\overline{k_{RES}}}{\overline{k_{RES}} + \overline{k_{SGS}}} \quad (8)$$

The subgrid-scale kinetic energy $\overline{k_{SGS}}$ was directly averaged during the LES calculation, while $\overline{k_{RES}}$ was evaluated at the end of the simulation, from the root mean square of the velocity fluctuations:

$$\overline{k_{RES}} = \frac{1}{2} \sum_{i=1}^{3} \overline{v}_{RMS,i}^2 \quad (9)$$

Figure 11 presents the solved kinetic energy fraction on a middle longitudinal plane of the test section, as a contour plot. It is evident that the spatial distribution of the mesh was adequate to solve for at least the 85% of turbulent kinetic energy in the vast majority of the domain.

The final thermal distribution on the ribbed surface obtained at the end of the last LES calculation is reported in Figure 12. The picture highlights a progressive temperature decrease from the inlet of the test section up to the end of the first inter-ribs interval. After that, an almost periodic distribution occurs as a consequence of the turbulent phenomena generated by the flow interaction with the ribs: a local maximum temperature close to the leeward side of the rib (where the flow is separated) establishes in each inter-ribs interval, while a local minimum value takes place mid-way between two successive ribs, corresponding to the location of the flow reattachment. The temperature then increases again before the next rib, because of the flow deceleration due to the potential effect of the obstacle. The temperature map was used to derive the Nusselt variation along the plate centerline, in accordance with the procedure followed by Tanda [15], using Eqs. (1) and (2). A comparison between the LES prediction and the experimental measurements is reported in Figure 13. The plot allows to appreciate the good agreement between the two curves. The numerical curve lies almost completely within the experimental uncertainty band. The only portions outside the band are at the extremes of the heated plate, where numerical boundary

conditions have some larger effect on the results (the extremes are treated as adiabatic in CFD simulations, while some heat transfer might exist in the experiment).

When compared to the results obtained from RANS simulations, the LES approach provided a significantly more accurate evaluation of the heat exchange along the plate centerline and in particular in the proximity of the ribs, where the RANS shell plate models (Figure 4a) showed to overestimate the decay in Nusselt number. Similarly, the better approximation of the turbulent flow components obtained from LES simulations allowed a netter estimation of the average Nusselt value with respect to the RANS thick plate prediction (Figure 4b). These improvements led to a sensible reduction in the deviation with respect to the experimental data, reducing the relative error to 4.39% on the average *Nu* (against 24.0% of the best RANS shell plate prediction) andto 5.88% on the Nu_{max} to Nu_{min} ratio (against 11.8% of the best RANS thick plate prediction), as summarized in Table 4.

Figure 14 reports a temporal sequence of the velocity field captured during the last airflow passage over the ribbed plate. It is possible to appreciate the presence of strong fluctuating components generated by the interaction of the flow stream with the ribs. Two flow regions coexist: a high velocity zone above the ribs, characterized by instantaneous local maximum values up to 10m/s, and a slower one, included in the inter-ribs spaces, where the flow separation causes wide recirculation areas. The regions preceding the flow reattachment represent stagnation zones for the flow and do not promote an efficient heat exchange.

Therefore, an accurate evaluation of the recirculation size is of primary importance to predict the thermal efficiency of ribbed surfaces, and this can be more easily estimated with reference to the average flow field. Figure 15 presents a superposition of the flow streamlines with the velocity

contours map, predicted by 3D LES and 2D RANS simulations with the different turbulence models considered. The LES velocity field, averaged over the last loop (corresponding to 3 flow passages), is captured on the mid longitudinal plane. This comparison confirms the good agreement between the different models in predicting the general flow behavior: the airflow approaches the test section along well-aligned parallel streamlines that begin to depart from the horizontal direction at a distance of about 3.5 rib heights before the first rib. Then, an acceleration occurs up to a peak velocity of about 8 m/s, just over the first inter-ribs space. A good agreement between the LES and the *k-ε* based RANS simulations is observed also for the size of the flow recirculation areas. On the contrary, *k-ω* models show a tendency to overestimate the flow separation length in all the inter-ribs regions, thus partially explaining the lower Nusselt values earlier observed in the curves of Figure 4.

The different predictions of Nusselt number distribution obtained from LES and RANS approaches can be explained by analyzing the turbulent kinetic energy predicted by the different models, as this is representative of the heat transfer due to turbulent convection. Figure 16 compares the average turbulent kinetic energy (sum of solved and modeled fractions) with the LES approach against the one modeled by the different RANS approaches. It is evident that the LES simulation captured a larger amount of turbulence, as confirmed by the achievement of peak values up to 6.6 m^2/s^2, especially in the proximity of the upper ribs face, that are not observable in the RANS results. The *k-ε* models produced large kinetic energy distributions predominantly in the bottom half of the channel, similar to the one predicted by the LES simulation, but characterized by lower average values. Instead, the *k-ω* models significantly underestimated turbulence values with respect to both the LES and *k-ε* models' group. As a further confirmation of the above considerations, Table 5 offers a numerical comparison among the mass-weighted average values for the turbulent kinetic

energy inside the test channel predicted by the different models. The LES approach provides the largest turbulence estimation while, among RANS models, the k-ε shows the lowest relative difference with respect to the LES result (46.0%). On the contrary, the maximum LES-RANS difference corresponds to 77.2% and was obtained with the SST k-ω turbulence model.

The contribution of turbulence in promoting the thermal mixing, and hence the effectiveness of the heat exchanger, can be better appreciated in Figure 17, where the 3D LES streamlines colored with the flow temperature are shown together with the Nusselt distribution on the plate. The air that flows over the first three ribs maintains an ordered behavior, thus allowing the development of a vertical thermal gradient, which is typical of a predominantly conductive heat exchange. After the third rib, the turbulence intensification, originated by the progressive interaction with the ribs, gradually propagates to all flow levels, enabling the transition to a highly convective heat transfer regime. A more uniform temperature distribution is therefore observed in the airflow approaching the exit from the test section. Similarly, the average Nusselt number distribution on the ribbed surface increases from the inlet ($Nu \approx 60$) to the outlet section (up to about 80). Within each inter-ribs space, the lowest Nu value is found in the recirculation zone, while a local maximum occurs where the flow reattaches.

Finally, the Q-criterion [44] was applied to the LES results aiming to identify the vortical structures inside the test section. Figure 18 reports the distribution of the iso-surfaces associated to a Q value of $5 \cdot 10^6 s^{-2}$, colored with the velocity magnitude, at the final time instant of loop 2 ($t = 1.44\,s$) and loop 3 ($t = 1.92\,s$). The sequence allows to confirm the effectiveness of the ribs in promoting the turbulence generation, attested by a large number of vortices detaching from their upper surface and that are further sustained by the flow recirculation occurring in each inter-ribs space.

Conclusions

The thermal performance of a rib-roughened plate equipped with transverse continuous ribs was evaluated by means of CFD simulations based on 2D steady RANS and 3D LES approaches. Particular attention was dedicated to the role that a detailed modelling of the heat exchange through the steel plate may have on the accuracy of the performance estimation. Therefore, in RANS simulations, the plate used in the experiment to provide the heating to the fluid was represented both using zero-thickness and real-thickness approaches. In accordance to previous published studies, when the heat flux is applied directly to the fluid domain, all the simulations performed with the different turbulence models predict a variability in Nusselt number significantly larger than in the experiments, with a good agreement only in the central region between successive ribs. On the contrary, when the heat flux is applied to the bottom of the steel plate, the variability in Nusselt number has a trend remarkably similar to the experiments, but with significantly lower absolute values.

The same problem was then simulated with a LES approach, to verify whether the low values of Nusselt number from RANS simulation could have been caused by an underestimation of turbulent convection. The simulation of the heat transfer in both the solid and fluid domain was achieved by means of an iterative procedure, which allowed to obtain a distribution of Nusselt number remarkably close to the experimental data. The results presented in this work demonstrate the importance of both a correct representation of the experimental setup and turbulence modeling for the estimation of the heat transfer in ribbed channels. The simulation of the thermal diffusion inside the plate allows the heat transfer to the fluid to be more representative of the experiment, with the effect of a more even temperature distribution on the upper plate surface. Finally, the use of a

higher-fidelity turbulence model (LES) allowed a better estimation of the turbulent energy production and therefore of the heat transfer within the fluid.

Conflict of interest

None to declare

Acknowledgments

This project has received funding from the Regione Autonoma della Sardegna within the project "Heated-Air Plug&Play" (project code RICERCA_1C-83).

Nomenclature

C	Correlation coefficient (-)
CFD	Computational Fluid Dynamics
c_p	Specific heat at constant pressure (J/kg K)
D_h	Hydraulic diameter (m)
e	Rib height (m)
er	Relative error (-)
exp	Experimental
ext	Extrapolated

GCI	Grid convergence index (-)
h	Convective heat transfer coefficient (W/m^2K)
H	Channel height (m)
i	x, y, z-components
k	Turbulent kinetic energy (m^2/s^2)
k_l	Solved fraction of turbulent kinetic energy (-)
L	Correlation length (m)
l_0	Integral length scale (m)
LES	Large Eddy Simulation
max	Maximum value
min	Minimum value
Nu	Nusselt number (-)
Nu_w	Average wall Nusselt number (-)
$Nu_{w,\infty}$	Asymptotic Average wall Nusselt number (-)
p	Rib pitch (m)
p_c	Convergence order
$\dot{q}_i$	Heat flux (boundary condition) (W/m^2)

$\dot{q}_w$	Wall heat flux per unit area (W/m^2)
$\dot{Q}_{¿}$	Heat flux (boundary condition) (W)
$\dot{Q}_w$	Wall heat flux (W)
R	Spatial correlation of velocity (m^2/s^2)
RANS	Reynolds-averaged Navier-Stokes equations
$\Re$	Reynolds number (-)
RES	Directly solved
RMS	Root mean square
RNG	Renormalization Group
RSM	Reynolds Stress Model
s	Distance (m)
SGS	Subgrid-scale
SST	Shear Stress Transport
$T_{air,x}$	Air bulk temperature (K)
t	Time (s)
TLCs	Thermochromic liquid crystals
tr	Time scale ratio (-)

T_w	Local temperature on ribbed plate (K)
v	Velocity (m/s)
VG	Vortex Generators
W	Width of the LES domain (m)
x	axial position (m)
$\vec{x}$	Generic point of the numerical domain (m)
y	Vertical position (m)
$y^{+¿¿}$	Dimensionless wall distance (-)
$\vec{w}$	Unit vector in the transverse direction
α	Thermal diffusivity (m^2/s)
ε	Turbulent kinetic energy dissipation rate (m^2/s^3)
κ	Thermal conductivity of air (W/mK)
λ	Thermal conductivity of solid (W/m K)
μ	Dynamic viscosity (kg/m s)
ρ	Density (kg/m^3)
τ	Integration period (s)
τ_w	Wall shear stress (N/m^2)

ω Turbulent kinetic energy specific dissipation rate (1/s)

References

[1] B. W. Webb, and S. Ramadhyani. *"Conjugate heat transfer in a channel with staggered ribs", International Journal of Heat and Mass Transfer,* vol. 28, no. 9, pp. 1679-1687, Sep. 1985. DOI: 10.1016/0017-9310(85)90142-5

[2] M. Sheikholeslami, M. Goji-Bandpy, and D. D. Ganji, *"Review of heat transfer enhancement methods: Focus on passive methods using swirl flow devices", Renewable and Sustainable Energy Reviews*, vol. 49, pp. 444-469, Sep. 2015. DOI: 10.1016/j.rser.2015.04.113

[3] R. J. Goldstein *et al.*, *"Heat transfer - A review of 2004 literature", International Journal of Heat and Mass Transfer*, vol. 53, no. 21-22, pp. 4343-4396, Oct. 2010. DOI: 10.1016/j.ijheatmasstransfer.2010.05.004

[4] S. K. Jain, G. D. Agrawal, and R. Misra, *"A detailed review on various V-shaped ribs roughened solar air heater*", *Heat and Mass Transfer*, vol. 55, no. 12, pp. 3369-3412, 2019. DOI: 10.1007/s00231-019-02656-4

[5] B. Yang, T. Gao, J. Gong, and J. Li, *"Numerical investigation on flow and heat transfer of pulsating flow in various ribbed channels", Applied Thermal Engineering*, vol. 145, pp. 576-589, Dec. 2018. DOI: 10.1016/j.applthermaleng.2018.09.041

[6] J. Wang, J. Liu, L. Wang, B. Sundèn, and S. Wang, *"Numerical investigation of heat transfer and fluid flow in a rotating rectangular channel with variously-shaped discrete ribs", Applied Thermal Engineering*, vol. 129, pp. 1369-1381, Jan. 2018. DOI: 10.1016/j.applthermaleng.2017.09.142

[7] Ye-Di Liu, L. A. Diaz, and N. V. Suryanarayana. *"Heat transfer enhancement in air heating fiat-plate solar collector*s". Trans. ASME, J. of Solar Energy Eng., vol. 106, pp. 358-363, Aug. 1984. DOI: 10.1115/1.3267608

[8] B. N. Prasad, and J. S. Saini, *"Effect of artificial roughness on heat transfer and friction factor in a solar air heater"*. Solar Energy, vol. 41, no. 6, pp. 555-560, 1988. DOI: 10.1016/0038-092X(88)90058-8

[9] B. N. Prasad, and J. S. Saini, *"Optimal thermohydraulic performance of artificially roughened solar air heaters"*. Solar Energy, vol. 47, no. 2, pp. 91-96, 1991. DOI: 10.1016/0038-092X(91)90039-Y

[10] R. L. Webb, *"Heat transfer and friction in tubes with repeated-rib roughness"*. International Journal of Heat and Mass Transfer, vol. 14, no. 4, pp. 610-617, Apr. 1971. DOI: 10.1016/0017-9310(71)90009-3

[11] S. K. Verma, and B. N. Prasad, "Investigation for the optimal thermohydraulic performance of artificially roughned solar air heaters". Renewable Energy, vol. 20, no. 1, pp. 19-36, May 2000. DOI: 10.1016/S0960-1481(99)00081-6

[12] T. Chompookham, C. Thianpong, S. Kwankaomeng, and P. Promvonge, *"Heat transfer augmentation in a wedge-ribbed channel using winglet vortex generators"*. International Communications in Heat and Mass Transfer, vol. 37, no. 2, pp. 163-169, Feb. 2010. DOI: 10.1016/j.icheatmasstransfer.2009.09.012

[13] T. Hagari T., K. Ishida, T. Oda, Y. Douura, and Y. Kinoshito, *"Heat Transfer and Pressure Losses of W-Shaped Small Ribs at High Reynolds Numbers for Combustor Liner"*. Journal of Engineering for Gas Turbines and Power, vol. 133, no. 9, paper number 091901, 8 pages, Sep. 2011. DOI: 10.1115/1.4002878

[14] Y. Li, Y. Rao, D. Wang, P. Zhang, and X. Wu, *"Heat transfer and pressure loss of turbulent flow in channels with miniature structured ribs on one wall", International Journal of Heat and Mass Transfer*, vol. 131, pp 584-593, Mar. 2019. DOI: 10.1016/j.ijheatmasstransfer.2018.11.067

[15] G. Tanda, *"Heat transfer in rectangular channels with transverse and V-shaped broken ribs", International Journal of Heat and Mass Transfer*, vol. 47, no. 2, pp. 229-243, Jan. 2004. DOI: 10.1016/S0017-9310(03)00414-9

[16] L. Baggetta, F. Satta, and G. Tanda, *"A Possible Strategy for the Performance Enhancement of Turbine Blade Internal Cooling With Inclined Ribs"*, *Heat Transfer Engineering*, vol. 40, no. 1-2, pp. 184-192, Jan. 2018. DOI: 10.1080/01457632.2017.1421305

[17] F. Satta, G. Tanda, and G. Venturino, *"Effect of Entrance Geometry on Heat Transfer in a Rib-Roughened Rectangular Channel", Heat Transfer Engineering*, vol. 43, no. 7, pp. 623-637, 2022. DOI: 10.1080/01457632.2021.1896836

[18] J. Liu *et al.*, *"Application of fractal theory in the arrangement of truncated ribs in a rectangular cooling channel (4:1) of a turbine blade", Applied Thermal Engineering*, vol. 139, pp. 488-505, Jul. 2018. DOI: 10.1016/j.applthermaleng.2018.04.133

[19] Y. Rao, and P. Zhang, *"Experimental Study of Heat Transfer and Pressure Loss in Channels with Miniature V Rib-Dimple Hybrid Structure"*, Heat Transfer Engineering, vol. 41, pp. 1431-1441, 2020. DOI: 10.1080/01457632.2019.1628502

[20] N. Kaewchoothong, K. Maliwan, K. Takeishi, and C. Nuntadusit, *"Effect of inclined ribs on heat transfer coefficient in stationary square channel", Theoretical & Applied Mechanics Letters*, vol. 7, no. 6, pp. 344-350, Nov. 2017. DOI: 10.1016/j.taml.2017.09.013

[21] Ma C., Ji Y., Zang S., and Chen H., *"An experimental study on convective heat transfer performance of steam and air flow in V-shaped rib roughened channels", Experimental Heat Transfer*, vol. 32, no. 1, pp. 51-68, 2019. DOI: 10.1080/08916152.2018.1473529

[22] N. Kaewchoothong, T. Sukato, P. Narato, and C. Nuntadusit, *"Flow and heat transfer characteristics on thermal performance inside the parallel flow channel with alternative ribs based on photovoltaic/thermal (PV/T) system", Applied Thermal Engineering*, vol. 185, art. no. 116237, Feb. 2021. DOI: 10.1016/j.applthermaleng.2020.116237

[23] S. Eiamsa-ard, and W. Changcharoen, *"Analysis of Turbulent Heat Transfer and Fluid Flow in Channels with Various Ribbed Internal Surfaces", Journal of Thermal Science*, vol. 20, no. 3, pp. 260-267, 2011. DOI: 10.1007/s11630-011-0468-3

[24] A. Boulemtafes-Boukadoum, and A. Benzaoui, *"CFD based analysis of heat transfer enhancement in solar air heater provided with transverse rectangular ribs", Energy Procedia*, vol. 50, pp. 761-772, 2014. DOI: 10.1016/j.egypro.2014.06.094

[25] T. Ma *et al.*, "*Study on heat transfer and pressure drop performances of ribbed channel in the high temperature heat exchanger", Applied Energy*, vol. 99, pp. 393-401, Nov. 2012. DOI: 10.1016/j.apenergy.2012.05.030

[26] A. Akcayoglu, and C. Nazli, *"A Comprehensive Numerical Study on Thermohydraulic Performance of Fluid Flow in Triangular Ducts with Delta-Winglet Vortex Generators", Heat Transfer Engineering*, vol. 39, no. 2, pp. 107-119, 2018, DOI: 10.1080/01457632.2017.1288046

[27] E. Ali, J. Park, and H. Park, *"Numerical Investigation of Enhanced Heat Transfer in a Rectangular Channel with Winglets", Heat Transfer Engineering*, vol. 42, no. 8, pp. 695-705, 2021, DOI: 10.1080/01457632.2020.1723845

[28] Z. Wang, Y. Yin, L. Yang, Y. Wang, and Y. Luan, *"Similar Characteristics of Heat Transfer in Different Scale Cooling Channel with Ribs", Heat Transfer Engineering*, in press. DOI: 10.1080/01457632.2021.1932038

[29] A. Afzal, H. Chung, K. Muralidhar, and H. H. Cho, *"Neural-network-assisted optimization of rectangular channels with intersecting ribs for enhanced thermal performance," Heat Transfer Engineering*, vol. 41, no. 18, pp. 1609–1625, 2020. DOI: 10.1080/01457632.2019.1661693

[30] S. Chokphoemphun, P. Promthaisong, N. Pipatpaiboonm and N. Onsalung, *"Thermal Augmentation in a Force Convective Cabinet Dryer Using Zigzag Ribs Fitted on Air Heater Section", Heat Transfer Engineering*, vol. 42, no. 15, pp. 1249-1267, 2021. DOI: 10.1080/01457632.2020.1785695

[31] D. Zheng, X. Wang, and Q. Yuan, *"Numerical investigation on the flow and heat transfer characteristics in a rectangular channel with V-shaped slit ribs", Infrared Physics & Technology*, vol. 101, pp. 56-67, 2019. DOI: 10.1016/J.INFRARED.2019.06.00

[32] D. Zheng, X. Wang, and Q. Yuan, "*The flow and heat transfer characteristics in a rectangular channel with convergent and divergent slit ribs", International Journal of Heat and Mass Transfer*, vol. 141, pp. 464-475, Oct. 2019. DOI: 10.1016/j.ijheatmasstransfer.2019.06.060

[33] Y. Liu, P. G. Tucker, and G. Lo Iacono, *"Comparison of zonal RANS and LES for a non-isothermal ribbed channel flow", International Journal of Heat and Fluid Flow*, vol. 27, no. 3, pp. 391-401, Jun 2006. DOI: 10.1016/j.ijheatfluidflow.2005.11.004

[34] A. Bjerg, K. Christoffersen, H. Sørensen, and J. Hærvig, *"Flow structures and heat transfer in repeating arrangements of staggered rectangular winglet pairs by Large Eddy Simulations: Effect of winglet height and longitudinal pitch distance", International*

Journal of Heat and Mass Transfer, vol. 131, pp. 654-663, Mar. 2019. DOI: 10.1016/j.ijheatmasstransfer.2018.11.015

[35] A. Colleoni, A. Toutant, and G. Olalde, *"Simulation of an innovative internal design of a plate solar receiver: Comparison between RANS and LES results"*, *Solar Energy*, vol. 105, pp. 732-741, Jul. 2014. DOI: 10.1016/j.solener.2014.04.017

[36] E. Toubiana, R. Gautier, D. Bougeard, and S. Russeil, *"Large Eddy Simulation of transitional flows in an elliptical finned-tube heat exchanger"*, *International Journal of Thermal Sciences*, vol. 144, pp. 158-172, Oct. 2019. DOI: 10.1016/j.ijthermalsci.2019.05.002

[37] P. Peltonen, K. Saari, K. Kukko, V. Vuorinen, and J. Partanen, *"Large-Eddy Simulation of local heat transfer in plate and pin fin heat exchangers confined in a pipe flow"*, *International Journal of Heat and Mass Transfer*, vol. 134, pp. 641-655, May 2019. DOI: 10.1016/j.ijheatmasstransfer.2019.01.046

[38] F. Stern, R. V. Wilson, H. W. Coleman, and E. G. Paterson, *"Comprehensive approach to verification and validation of CFD simulations part 1: methodology and procedures"*, *Journal of Fluids Engineering*, vol. 123, no. 4, pp. 793–802, 2001. DOI: 10.1115/1.1412235

[39] I. B. Celik *et al.*, *"Procedure for estimation and reporting of uncertainty due to discretization in CFD applications"*, *Journal of Fluids Engineering*, vol. 130, no. 7, 2008. DOI: 10.1115/1.2960953

[40] J. C. Tyacke, and P. G. Tucker, *"Future use of Large Eddy Simulation in aero-engines"*, *Journal of Turbomachinery*, vol. 137, no. 8, paper no. 081005, 16 pages, Aug. 2015. DOI: 10.1115/1.4029363

[41] Ansys® Fluent, R15.0, User's guide, ANSYS, Inc., 2015

[42] Ansys® Fluent, R15.0, Theory guide, ANSYS, Inc., 2015

[43] L. Winchler *et al.*, *"Conjugate heat transfer methodology for thermal design and verification of gas turbine cooled components", Journal of Turbomachinery*, vol. 140, no. 12, paper no. 121001, 8 pages, Dec. 2018. DOI: 10.1115/1.4041061

[44] M. Lesieur , O. Métais, and P. Comte, *"Large-Eddy Simulations of Turbulence"*, Cambridge University Press, Cambridge. UK, 2005.

Table 1 – Grid convergence estimation

		Group 1	**Group 2**	**Group 3**	**Group 4**
Mesh size	*N1*	14,000	33,508	74,826	168,466
	N2	33,508	74,826	168,466	377,942
	N3	74,826	168,466	377,462	855,372
$\overline{Nu}_1/\overline{Nu}_{ext}$		1.0267	1.0109	1.0033	1.0084
$\overline{Nu}_2/\overline{Nu}_{ext}$		1.0113	1.0047	1.0006	1.0040
$\overline{Nu}_3/\overline{Nu}_{ext}$		1.0051	1.0020	1.0001	1.0019
p_c		2.27	2.05	4.23	2.05
GCI_1		2.773%	1.016%	0.092%	0.079%
GCI_2		1.175%	0.438%	0.016%	0.033%
GCI_3		0.533%	0.187%	0.003%	0.014%

Table 2 – Analysis of Nusselt values on the plate centerline predicted with different turbulence models, for the shell plate and the thick plate approach and comparison against the experimental values [15].

	Average Nu in the range 3 ≤ x/Dh ≤ 8.45		**|er%| on average Nu$^{(I)}$**		**Nu_{max}/Nu_{min} in the range 3 ≤ x/Dh ≤ 8.45**		**|er%| on $Nu_{max}/Nu_{min}^{(II)}$**	
Experimental [15]	68.4		-		1.19		-	
Turbulence model	**Shell plate**	**Thick plate**	**Shell plate**	**Thick plate**	**Shell plate**	**Thick plate**	**Shell plate**	**Thick plate**
k-ε	51.8	46.0	24.3	32.7	2.77	1.33	132.8	11.8
RNG k-ε	52.0	46.6	24.0	31.9	2.78	1.33	133.6	11.8
Realizable k-ε	47.5	42.2	30.6	38.3	3.27	1.39	174.8	16.8
k-ω	44.2	39.4	35.4	42.4	5.60	1.44	370.6	21.0
SST k-ω	42.4	38.7	38.0	43.4	4.72	1.36	296.6	14.3

(I) $¿er\,\% \vee ¿ \left| \frac{\overline{Nu}_{\exp} - \overline{Nu}_{CFD}}{\overline{Nu}_{\exp}} \right| \cdot 100$

(II) $¿er\,\% \vee ¿ \left| \frac{\left(\frac{\overline{Nu}_{max}}{\overline{Nu}_{min}}\right)_{\exp} - \left(\frac{\overline{Nu}_{max}}{\overline{Nu}_{min}}\right)_{CFD}}{\left(\frac{\overline{Nu}_{max}}{\overline{Nu}_{min}}\right)_{\exp}} \right| \cdot 100$

Table 3 – Average heat flux and correlation length as function of the domain width.

W/H	**Average heat flux [W/m^2]**	**L/H**
1	315.6	0.050
2	363.1	0.087
4	365.2	0.088

Table 4 –Nu trend analysis on the plate centerline predicted by LES. Comparison against the experimental values [15].

	Average Nu in the range 3 ≤ x/Dh ≤ 8.45	**|er%| on average Nu[(1)]**	**Nu_{max}/Nu_{min} in the range 3 ≤ x/Dh ≤ 8.45**	**|er%| on Nu_{max}/Nu_{min}[(2)]**
Experimental [15]	68.4	-	1.19	-
LES thick plate	71.4	4.39	1.12	5.88

(I) $¿er\,\% \vee ¿ \left| \frac{\overline{Nu}_{\exp} - \overline{Nu}_{CFD}}{\overline{Nu}_{\exp}} \right| \cdot 100$

(II) $¿er\,\% \vee ¿ \left| \frac{\left(\frac{\overline{Nu}_{max}}{\overline{Nu}_{min}} \right)_{\exp} - \left(\frac{\overline{Nu}_{max}}{\overline{Nu}_{min}} \right)_{CFD}}{\left(\frac{\overline{Nu}_{max}}{\overline{Nu}_{min}} \right)_{\exp}} \right| \cdot 100$

Table 5 – Comparison between the mass weighted average values of the turbulent kinetic energy predicted by LES and RANS approaches in the test channel.

	Average turbulent kinetic energy (m^2/s^2)(I)	**ΔTKE (%) (LES vs. RANS)**
LES	1.89	-
k-ε	1.02	-46.0
RNG k-ε	0.926	-51.0
Realizable k-ε	0.841	-55.5
k-ω	0.499	-73.6
SST k-ω	0.431	-77.2
(I) Mass weighted average value		

List of Figures

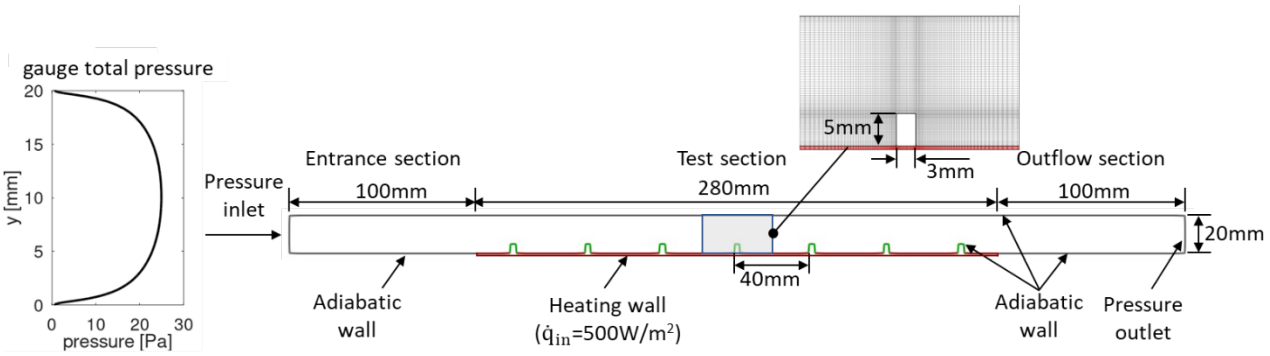

Figure 1 – Geometrical domain for the 2D RANS simulations, with a detail of the computational grid close to the ribs.

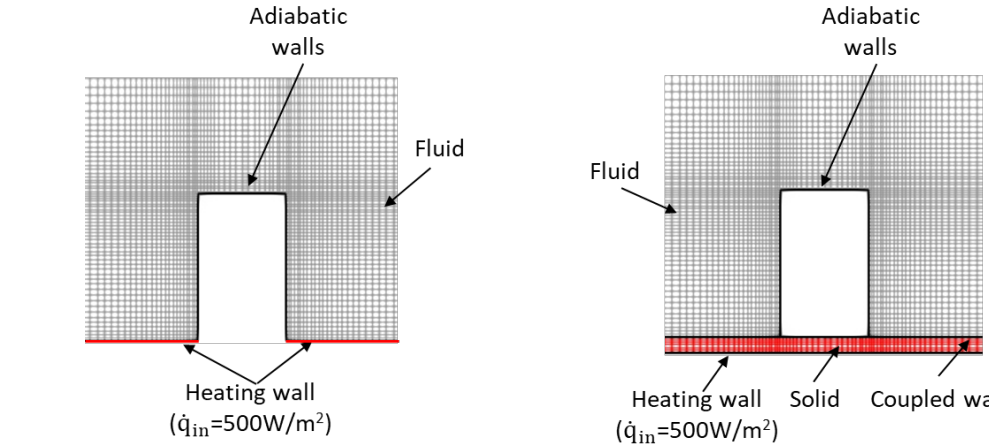

Figure 2 – Comparison between the RANS approaches: a) shell plate and b) thick plate.

a)

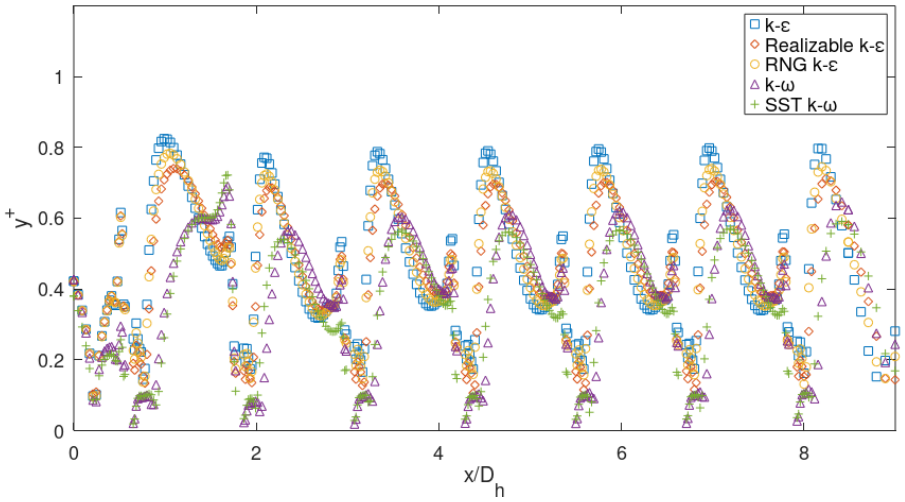

b)

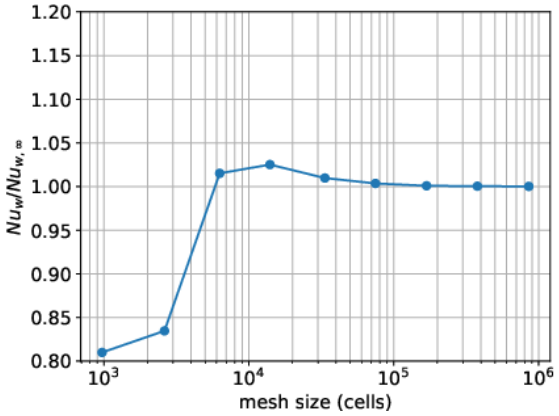

c)

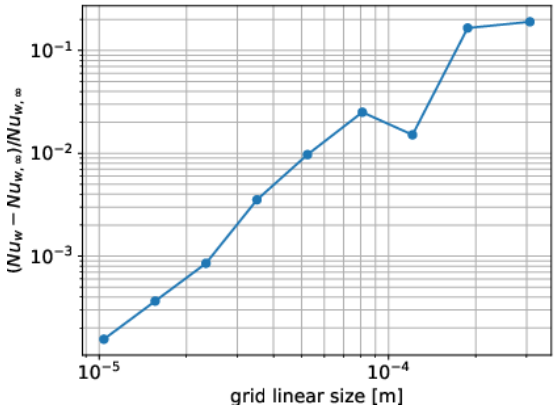

Figure 3 – Verification of the computational grid: a) y^+ along the heated surface of the selected mesh for different turbulence models; b) Nusselt number as a function of mesh size (SST $k-\omega$ model); c) relative error for the Nusselt number evaluation (SST $k-\omega$ model).

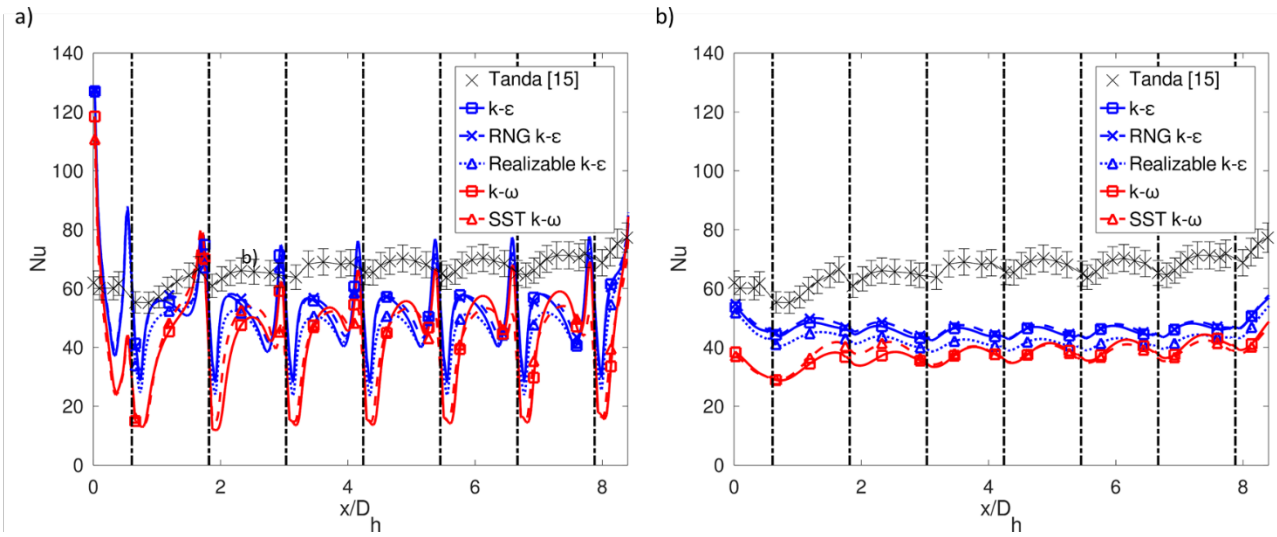

Figure 4 – Comparison of the local Nu along the plate centerline; experimental [15] against a) RANS shell plate approach and b) RANS thick plate approach.

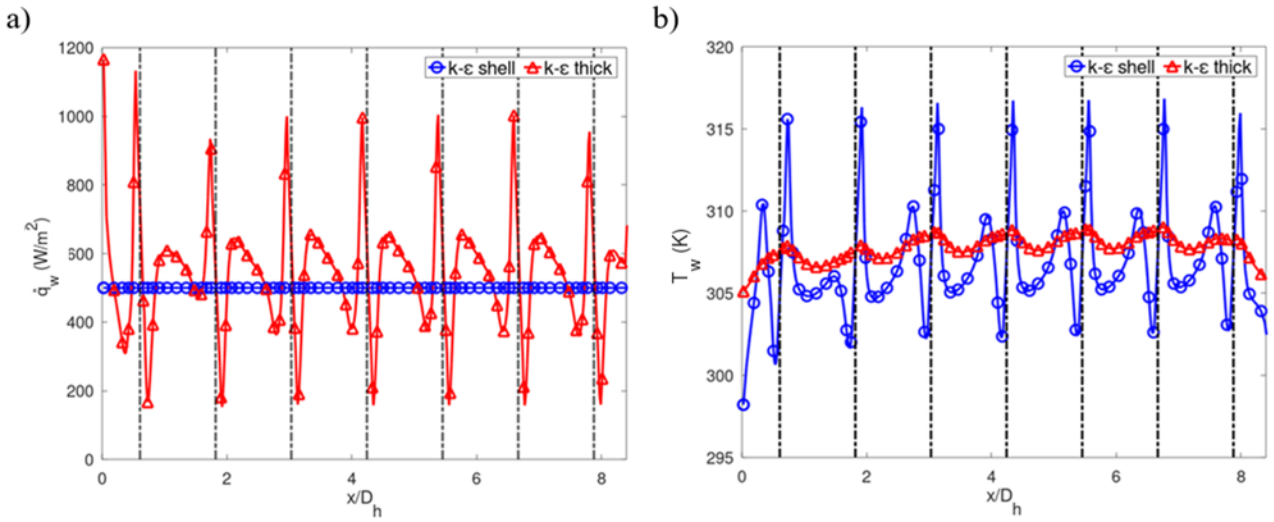

Figure 5 – Comparison between the shell plate and the thick plate approaches in terms of a) local heat flux and b) local wall temperature on the plate; simulation performed with the k-ε turbulence model.

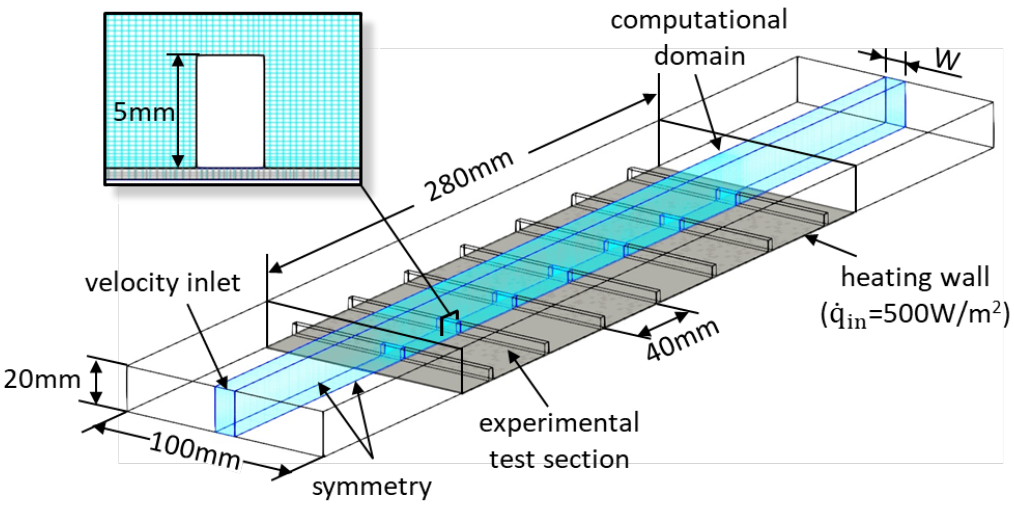

Figure 6 – Geometry of the experimental test section and of the computational domain for LES simulations.

a) b)

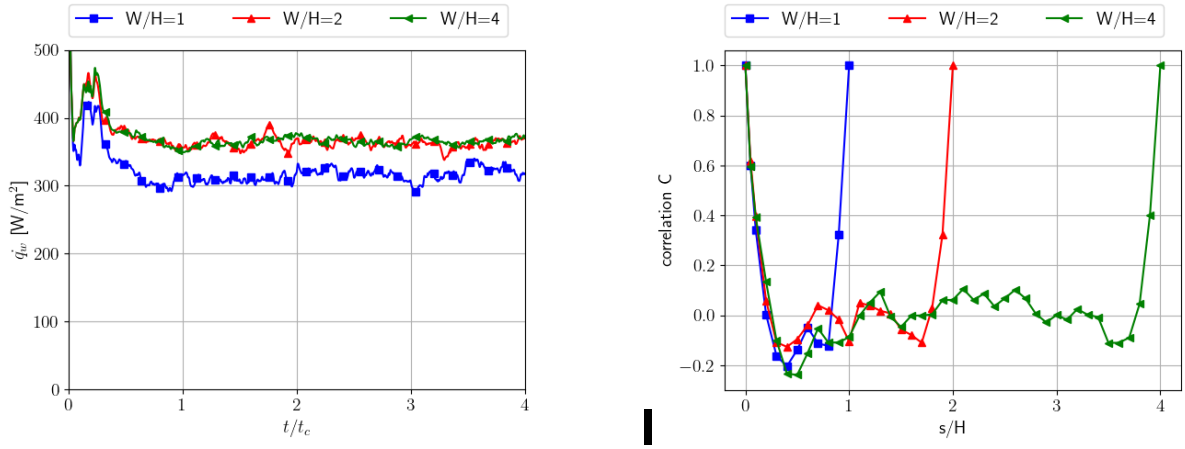

Figure 7 – Results of the sensitivity analysis on the domain width: a) heat transfer from the lower wall, b) cross-correlation in the transverse direction.

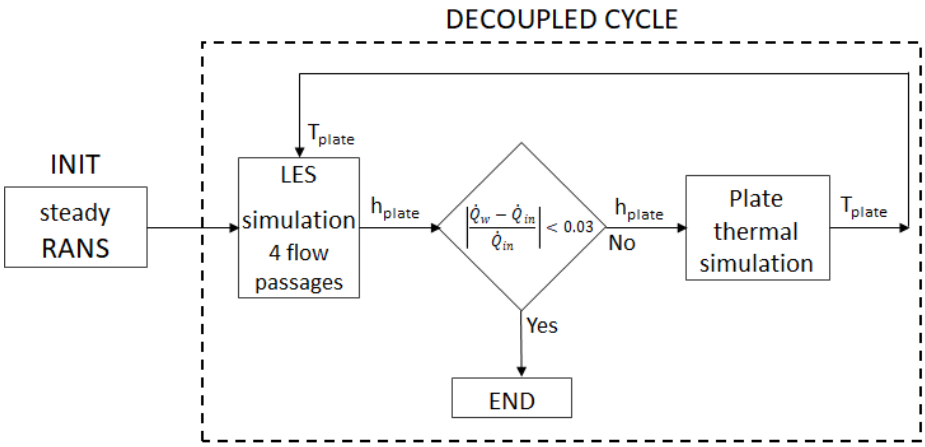

Figure 8 – Block diagram of the multi-step decoupled procedure.

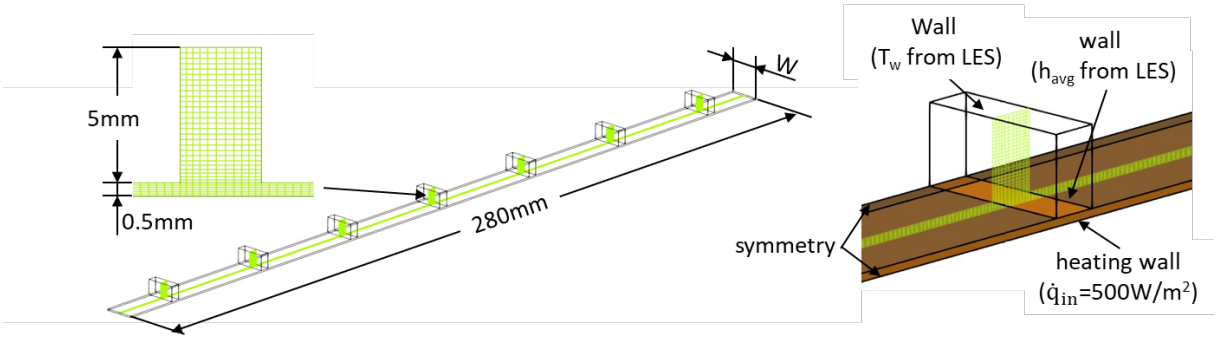

Figure 9 – Solid domain and computational grid of the ribbed steel plate; detail of the boundary conditions.

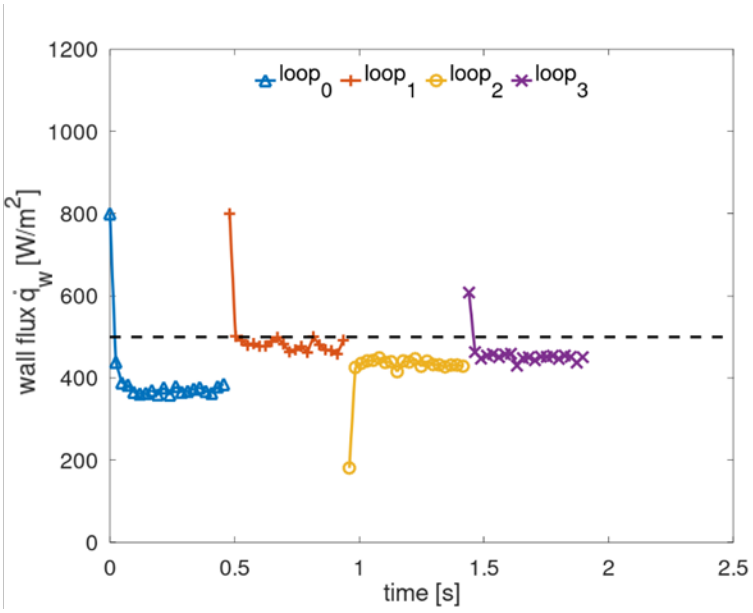

Figure 10 – Convergence diagram of the multi-step decoupled procedure.

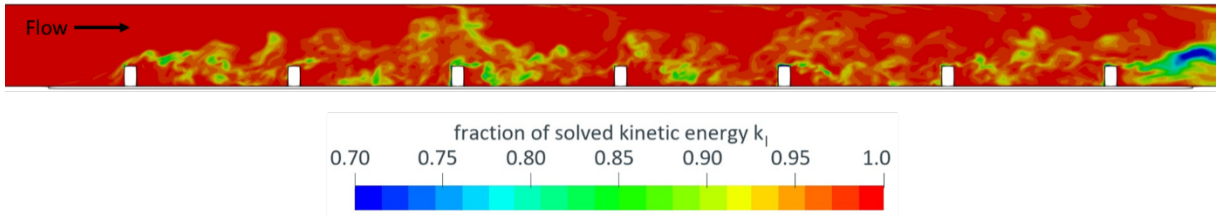

Figure 11 – Contour map of the solved kinetic energy fraction k_l

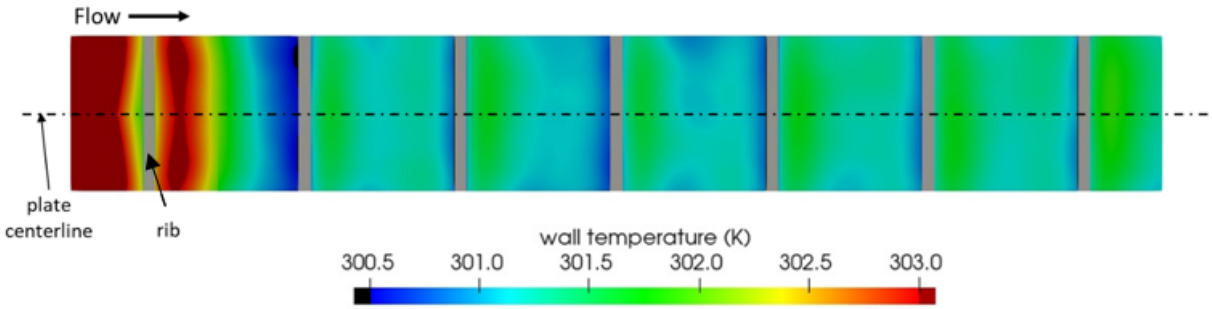

Figure 12 – Temperature distribution on the ribbed surface of the plate; LES thick plate approach.

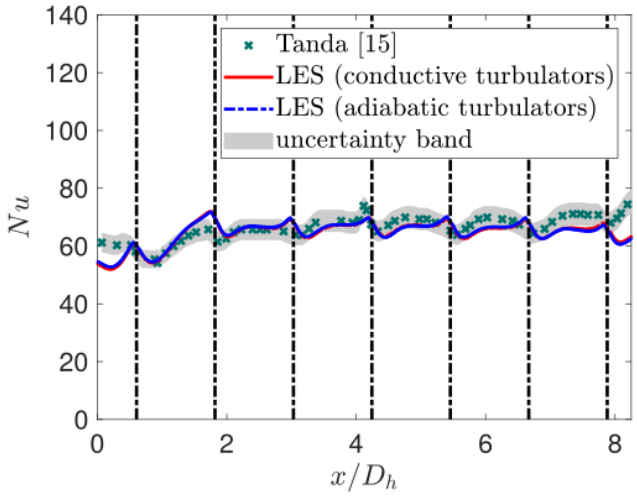

Figure 13 – Comparison of the local Nusselt number along the plate centerline; experimental [15] against LES thick plate approach; ribs were modeled both as adiabatic and as a low conductivity material

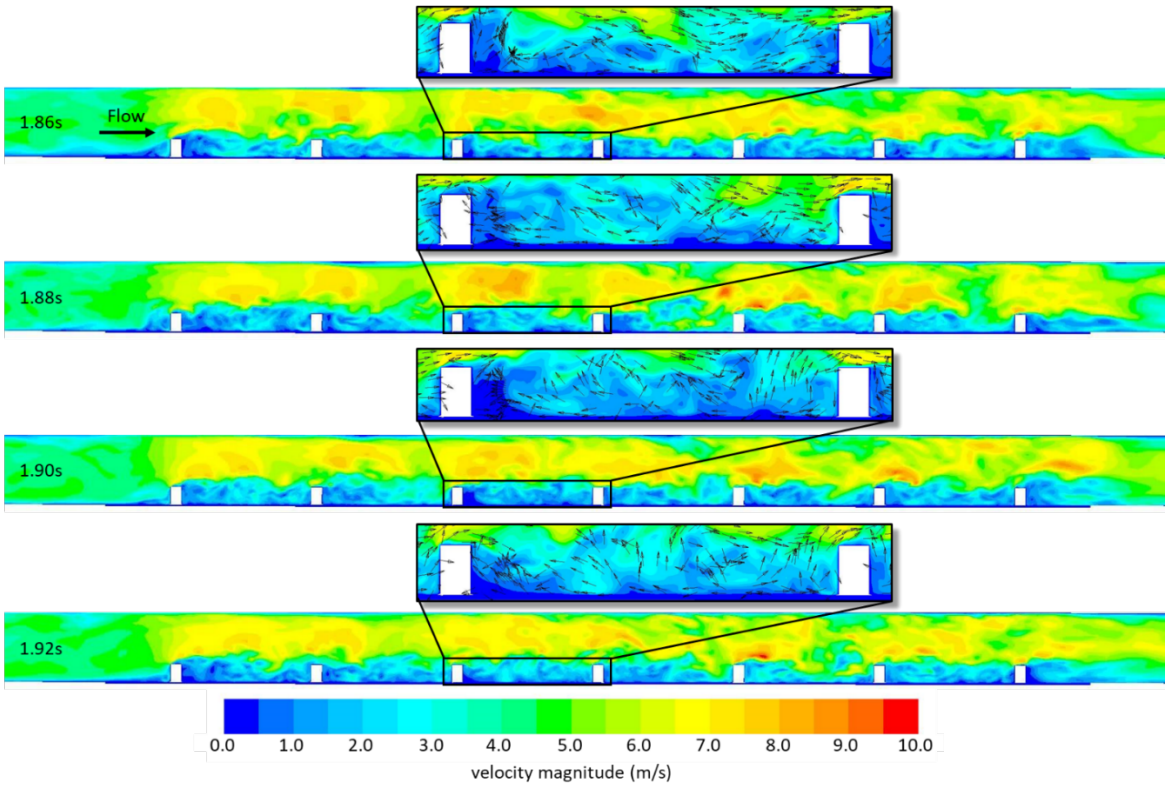

Figure 14 – LES velocity field at different time instants.

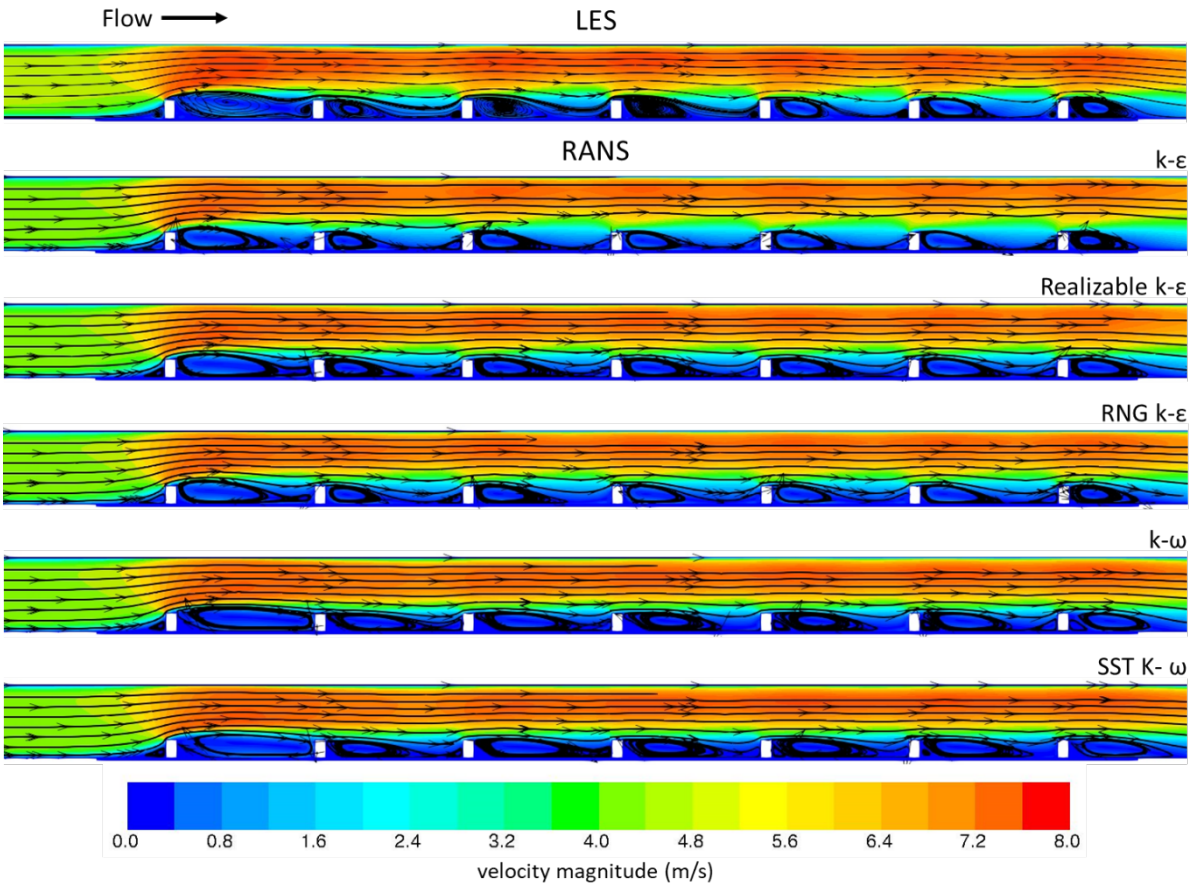

Figure 15 –Flow streamlines and mean velocity field: comparison between 3D LES and 2D RANS with different turbulence models.

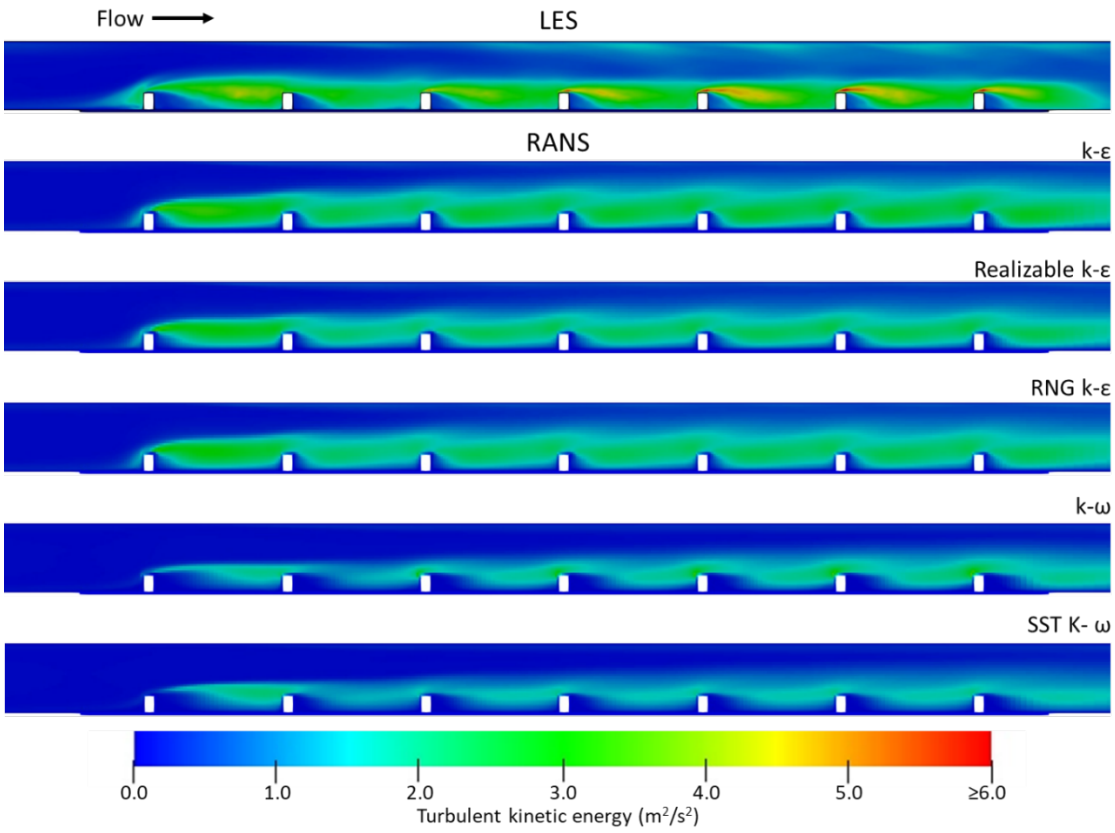

Figure 16 – Turbulent kinetic energy field: comparison between 3D LES and 2D RANS with different turbulent models.

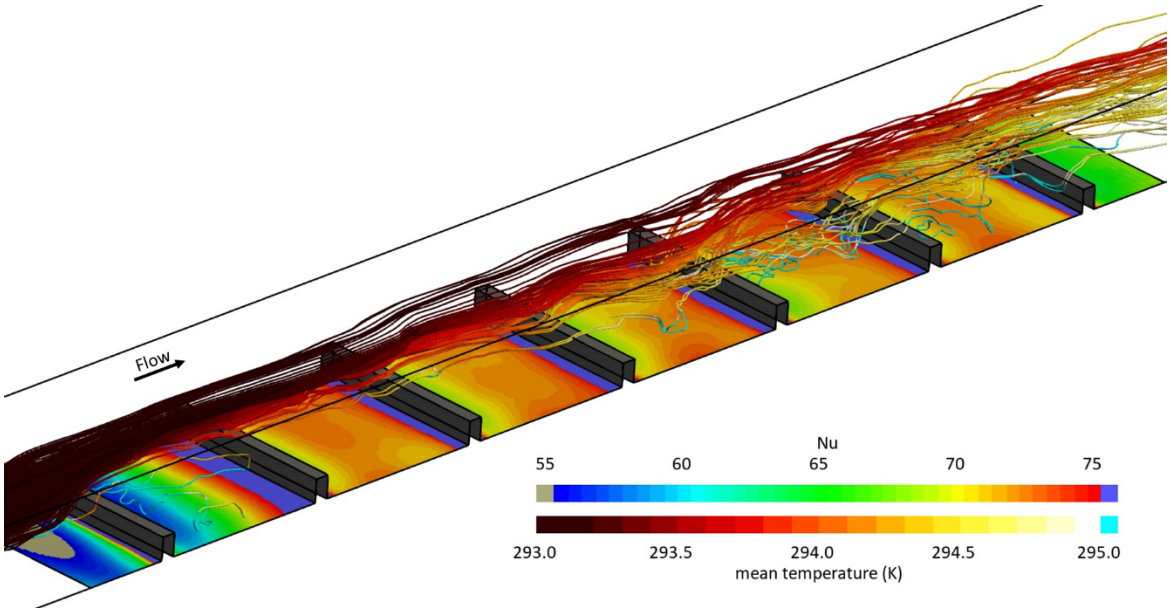

Figure 17 – Flow streamlines colored with the temperature and Nu distribution on the ribbed surface; LES results.

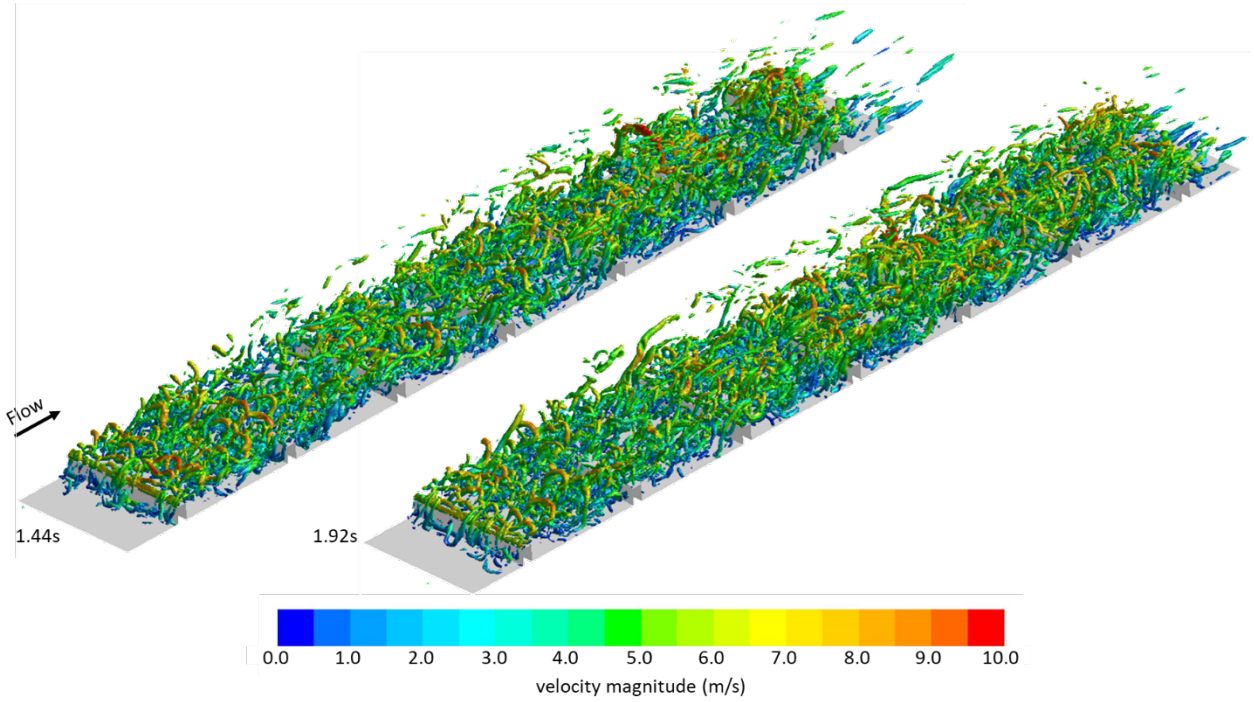

Figure 18 – Q-criterion analysis. Vortical structures colored with the velocity field magnitude at different time instants.

Authors Bios

Marco Bertoli obtained his Batchelor and Masters' Degree in Mechanical Engineering from the University of Cagliari. He collaborated with the Centro Sviluppo Materiali (CSM) - Structural Integrity and Reliability Department until 2015, mainly involved on fluid dynamics issues related to the oil&gas transportation in pipelines. His research activities were devoted to the study of the ductile fracture propagation, focusing on gas decompression behaviour for the driving force evaluation, as part of research projects funded by European Community (SARCO2 and INDUSE2). In 2015, he founded Astarte Strategies, a spin-off of the University of Cagliari which offers consultancy services for technological innovation of industrial products and processes. In Astarte, Marco is specialist in numerical and experimental methods. His main activities are focused on modeling, analysis and optimization of heat exchange processes as well as combustion, internal flows, aerodynamics and environmental dispersion of pollutants. Marco is also expert in biomed/vascular 3D modeling and simulation.

Francesco Cambuli obtained a degree in Mechanical Enigeering in 1994 and a Ph.D. in Mechanical Design in 1998, both from the University of Cagliari (Italy). Since January 2022 he is an Associate Professor at the Department of Mechanical, Chemical and Materials Engineering (DIMCM), University of Cagliari. His research activities are focused on the field of turbomachinery, developed with experimental and numerical (CFD) methods. Currently, the main topics are the aerodynamic analysis of Wells turbines, the study of the aerothermal behaviour of gas turbine blades and the performance evaluation of commercial pumps when used as turbines.

Roberto Baratti is Full Professor at the Department of Mechanical, Chemical and Materials Engineering, University of Cagliari. He obtained the Laurea degree (summa cum laude) from University of Cagliari in 1982 and the Dottorato di Ricerca (Ph.D.) from University of Pisa in 1986. Presently, his interests are in the field of process modeling and control of industrial processes and stochastic modeling of chemical, biochemical reactor.

Tiziano Ghisu is an Associate Professor at the Department of Mechanical, Chemical and Materials Engineering, University of Cagliari. He obtained a Masters' degree in Aerospace Engineering from the University of Turin, a Masters' degree from the University of Cranfield and a PhD from the University of Cambridge. His main research interests cover the numerical simulation of complex fluid dynamics problems through high-performance computing, the development and application of optimisation methods to problems of industrial relevance, uncertainty quantification and optimisation in presence of uncertainty. He is Principal Investigator for the Cagliari Unit in the projects Madeleine and NextAir, funded by the European Union through the Horizon 2020 Program.